Room Temperature Spin-Orbit Torque Switching Induced by a Topological Insulator

by
Jiahao Han
B.E., Tsinghua University (2016)

Submitted to the Department of Electrical Engineering and Computer Science
in Partial Fulfillment of the Requirements for the Degree of
Master of Science
at the
MASSACHUSETTS INSTITUTE OF TECHNOLOGY
September 2018

Signature redacted

Signature of Author .....
Department of Electrical Engineering and Computer Science
August 31, 2018

Signature redacted

Certified by ....
Luqiao Liu
Assistant Professor of Electrical Engineering and Computer Science
Thesis Supervisor

Signature redacted

Accepted by ....
Leslie A. Kolodziejski
Professor of Electrical Engineering and Computer Science
Chair, Department Committee on Graduate Students

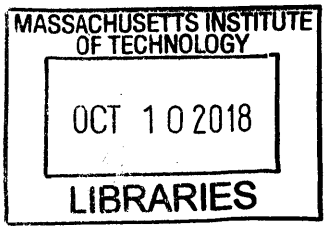

ARCHIVES

Room Temperature Spin-Orbit Torque Switching Induced by a Topological Insulator

by
Jiahao Han
B.E., Tsinghua University (2016)

Submitted to the Department of Electrical Engineering and Computer Science
on August 31, 2018 in Partial Fulfillment of the Requirements for
the Degree of Master of Science in
Electrical Engineering and Computer Science

ABSTRACT

Recent studies on the topological insulators have attracted great attention due to the rich spin-orbit physics and promising applications in spintronic devices. The strongly spin-moment coupled electronic states have been extensively pursued to realize efficient spin-orbit torque switching. However, so far current-induced magnetic switching with topological insulators has been observed only at cryogenic temperatures. Whether the topologically protected electronic states in topological insulators can benefit to spintronic applications at room temperature remains a controversial issue.

In this thesis, spin-orbit-torque-induced magnetic switching is realized in topological insulator/ferrimagnet heterostructure at room temperature. Ferrimagnetic CoTb alloy with robust bulk perpendicular magnetic anisotropy is directly grown on a classical topological insulator Bi_2Se_3. The low switching current density provides definitive proof of the high spin-orbit torque efficiency from topological insulators. The comparison between Bi_2Se_3 and $(Bi,Sb)_2Te_3$ with less bulk conductivity suggests the surface states plays a significant role in generated the efficient spin-orbit torques. Furthermore, the effective spin Hall angle of topological insulators is determined to be several times larger than commonly used heavy metals. These results demonstrate the robustness of topological insulators as a spin-orbit torque switching material and provide an avenue towards applicable topological insulator-based spintronic devices.

Thesis Supervisor: Luqiao Liu
Title: Assistant Professor of Electrical Engineering and Computer Science

ACKNOWLEDGEMENTS

It is my great pleasure to be admitted by Department of EECS at MIT and work in Prof. Luqiao Liu's group. I would like to firstly thank my thesis supervisor, Prof. Luqiao Liu, who has taught me a great deal from the details in experiments to the exploration of significant research topics. It is his continuous guidance, support, and encouragement that leads me deeply to the fascinating field of spintronics and helps me overcome various difficulties in research. Moreover, his dedication in academics and optimistic attitude encourages me a lot in my research and daily life.

I would like to thank my labmates, Dr. Yabin Fan, Dr. Hailong Wang, Dr. Yanfei Wu, Saima A. Siddiqui, Joseph Finley, Justin T. Hou, Taqiyyah Safi, and Pengxiang Zhang for their kind help in experiments and fruitful discussions. It is a wonderful time working with these friendly and talented people.

I want to thank the MTL/NSL staff members Kurt Broderick, Gary Riggott, and Mark Mondol. With their kind help and guidance, I can quickly work on the shared facilities and well arrange my experiments.

Finally, I want to express my deepest love and best wishes to my parents. Life as a graduate researcher at top institutions includes not only success and proudness, but also frustration and pressure. It is their love and trust that gives me courage to face the challenges and to pursue higher goals in my academic career.

Part of the results in this thesis have been published in Phys. Rev. Lett. 119, 077702 (2017).

TABLE OF CONTENTS

1 Introduction

The innovation in information technologies leads to the revolutionary changes of the life of human beings since early 20th century. The semiconductor-based devices, particularly the silicon-based transistors and the compound-metal-oxide-semiconductor (CMOS) devices, set up the foundation of modern electronic technologies and play a dominant role in industry. In most of the existing electronic devices, the flow of electron charge is utilized to generate, transport, and process information. However, the dramatic increase of the demand for information processing ask for higher density and the processing speed of devices, which adds challenges to the semiconductor fabrication techniques. Besides the charge of electrons, the eigenstates of the electron spin (up and down) that correspond to "0" and "1" signals provide novel degree of freedom for information storage and manipulation. Spin electronics (spintronics), where the electrons' spin degree of freedom is manipulated to interplay with electrical signals, stands out as a beyond-CMOS technology and is being actively developed in research and industry[1,2].

1.1 Giant magnetoresistance and tunneling magnetoresistance

The spins of electron and nuclei have been predicted theoretically and detected experimentally since the discovery of quantum mechanics in 1920s. However, the studies mainly focused on the magnetic responses of the spin angular momentum, while the interactions between charge and spin were not exploited. In 1988, Baibich *et al.*[3] and

Binash *et al.*[4] observed significant resistivity modulation by external magnetic field in magnetic multilayers, which is ascribed as the giant magnetoresistance (GMR) effect. A typical GMR device consisting ferromagnet 1/non-magnetic metal/ferromagnet 2 trilayer is named as spin valve and shown in Fig. 1.1. The resistivity can be switched between high and low values by the external field when the magnetization of the two ferromagnetic layers are parallel or anti-parallel.

The GMR effect can be interpreted using the spin-dependent scattering and double-current model. When the magnetization of the two ferromagnetic layers are parallel, the electrons whose spin magnetic moments are parallel with the ferromagnetic moments experience weak scattering when passing through the ferromagnetic layers, while the electrons with opposite spin orientation are strongly scattered. The overall resistance is low. The resistance changes dramatically when the two ferromagnetic layers are antiparallelly magnetized. The electrons with any spin orientation would be scattered intensively by one of the ferromagnetic layers, corresponding to high resistance state. The MR ratio of GMR devices can reach 50% at low temperature[3]. The magnetic storage and sensing devices based on the GMR effect has much higher sensitivity and signal-to-noise ratio compared the traditional magnetic devices based on the anisotropic magnetoresistance and have been successfully utilized in the production of high-density magnetic storage and sensing devices.

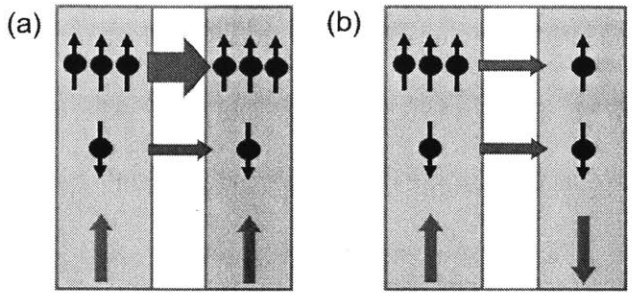

Fig. 1.1. Schematic of the GMR device structure in (a) parallel and (b) antiparallel configurations, corresponding to high and low resistance states, respectively. The bottom arrows show the magnetization derections.

Another important MR effect that is well adapted in industry is the tunneling magnetoresistance (TMR), the device structure of which is the magnetic tunnel junction (MTJ) consisting of ferromagnet 1/insulator/ferromagnet 2 sandwich structure[5-7]. The TMR has similar operation principles as the GMR device and its mechanism is described by the Julliere model[8] (Fig. 1.2). Note that the two sub-bands with opposite spin orientations in the ferromagnet have different density of states at the Fermi level, and the spin angular momentum of the electron is conserved after the tunneling. When the magnetization of the two ferromagnetic layers are parallel, the tunneled electrons from the major/minor sub-band of ferromagnet 1 occupy the major/minor sub-band of ferromagnet 2, resulting in a low resistance state. On the contrary, when the magnetization of the two ferromagnetic layers are antiparallel, the occupied electrons in the minor/major sub-band of ferromagnet 2 are the major/minor sub-band of ferromagnet 1. The total

number of the tunneled electrons are reduced, resulting in a high resistance state. In 2008, TMR with the ratio of >600% was realized in a CoFeB/single-crystalline MgO/CoFeB sandwiched junction, which benefits to the production of MTJs with ultrahigh stability and sensitivity[9].

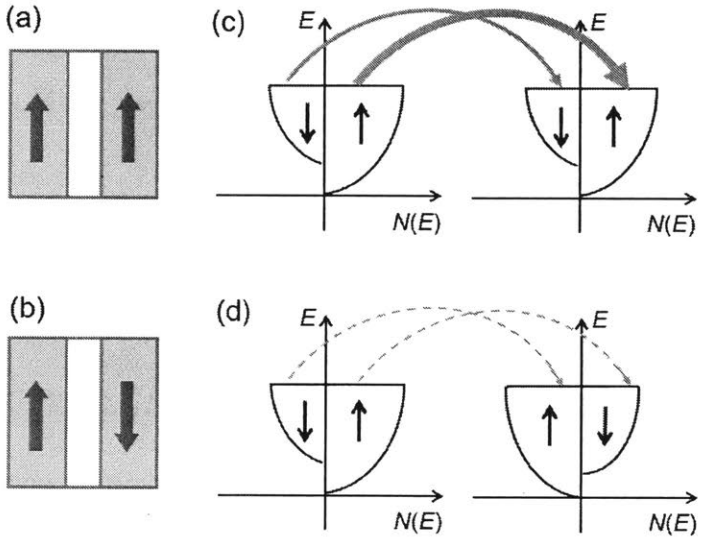

Fig. 1.2. Schematic of the TMR device structure and spin-polarized tunneling. (a) and (b) Device structure with parallel and antiparallel configurations. (c) and (d) Corresponding electron tunneling picture.

1.2 Spin transfer torques and spin-orbit torques

Despite the tremendous contributions GMR and TMR have made to the magnetic random access memory (MRAM) manufacture, the application of magnetic fields limits the device integration and causes significant power consumption. Alternatively, people

have explored the angular momentum transfer of electrons when a flow of charge current goes through a magnetic tunnel junction. The current with spins polarized by one ferromagnetic electrode can exert a torque onto the other ferromagnetic layer due to the conservation of the angular momentum and finally induce magnetic switching. This spin transfer torque effect[10,11] can significantly enhance the integration of devices because the charge current is highly localized. However, it is obvious that the flip of macroscopic magnetic materials requires a large number of spin-polarized electrons, which means the threshold current density for switching in order of $10^6 \sim 10^7$ A/cm^2 is usually required[12]. Whether the insulating layer can last long under such a large charge current becomes a significant issue[13].

The key to the current-induced magnetic switching is to generate high-density spin flow for sufficient angular momentum transfer. Besides the spin flow carried by the spin-polarized charge current, the pure spin current without any charge flow is an alternative origin of magnetic switching. This spin transfer torque comes from spin current or spin accumulation generated by the spin-orbit interactions and is therefore called the spin-orbit torque (SOT)[14-16]. In a heavy metal/ferromagnetic metal bilayer (Fig. 1.3), With current-induced nonequilibrium spin accumulation ($\boldsymbol{\sigma}$) in the ferromagnetic layer, spin torques are exerted onto the magnetic moments ($\boldsymbol{m}$), which can manipulate the magnetic dynamics and even switches the magnetization. The torques can be expressed as a field-like term $\boldsymbol{\tau}_{\mathrm{FL}} \sim \boldsymbol{\sigma} \times \boldsymbol{m}$ and a damping-like term $\boldsymbol{\tau}_{\mathrm{DL}} \sim \boldsymbol{m} \times (\boldsymbol{\sigma} \times \boldsymbol{m})$. Correspondingly, two

effective magnetic fields $\boldsymbol{H}_{\mathrm{FL}} \sim \boldsymbol{\sigma}$ and $\boldsymbol{H}_{\mathrm{DL}} \sim \boldsymbol{\sigma} \times \boldsymbol{m}$ can be introduced to describe the torques[17]. The MTJ based on the SOT does not require high-density charge current through the insulating layer, in contrast to traditional spin transfer torque devices[16].

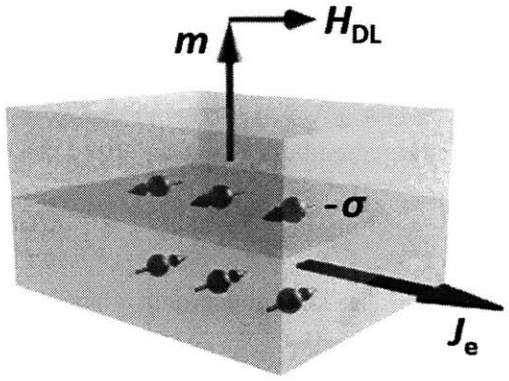

Fig. 1.3. Schematic of SOT in a heavy metal/ferromagnetic metal heterostructure. The charge current (j_e) generates spin accumulation ($-\boldsymbol{\sigma}$) which is perpendicular to the current direction at the interface and exerts a SOT on the magnetic moments ($\boldsymbol{m}$). The damping-like SOT is proportional to $\boldsymbol{m} \times (\boldsymbol{\sigma} \times \boldsymbol{m})$ and can be described by an effective field $\boldsymbol{H}_{\mathrm{DL}} \sim \boldsymbol{\sigma} \times \boldsymbol{m}$. Here, only the damping-like term is presented because it is mostly related to the magnetic switching.

1.3 Charge-to-spin conversion: spin Hall effect and Rashba effect

The generation of SOT by charge current requires charge-to-spin conversion and net spin accumulation, the most common mechanisms of which are the spin Hall effect[18-21] and the Rashba effect[22-25]. The spin Hall effect can be described by the schematic in Fig.

1.4(a). When a charge current flows through spin-orbit materials such as heavy metals (Pt, Ta, W, etc.), the electrons with opposite spins deflect in opposite directions, which results in a pure spin current in absence of charge flow. The spin current injected to the neighboring ferromagnetic layer can lead to net spin accumulation and the SOT on the magnetic moments. The directions of the charge current ($\boldsymbol{J}_e$), the spin current ($\boldsymbol{J}_s$), and the spin polarization ($\boldsymbol{\sigma}$) are perpendicular to each other, described as $\boldsymbol{J}_s = \alpha_{SH}(\hbar/2e)\boldsymbol{J}_e \times \boldsymbol{\sigma}$. Here $\hbar$ is the Plank's constant, e is the electron charge, and α_{SH} is the spin Hall angle defined to describe the charge-to-spin conversion ratio. Another important parameter in the spin Hall effect is the spin diffusion length (λ_{SD}), which is to describe the propagation distance of the electron when maintaining its spin polarization. λ_{SD} is usually in the order of nanometers in spin-orbit materials. The spin transport parameters of the commonly used heavy metals are summarized in Table 1.1.

Besides the spin Hall effect in three-dimension space, the interfacial Rashba effect is another origin of the SOT. Due to the Rashba spin-orbit coupling at the heavy metal/ferromagnetic metal interface, the spin and momentum of the electrons at the Fermi surface are locked with each other, forming two helical Fermi contours with opposite spin polarizations (Fig. 1.4(b))[22-25]. When a charge current flows through this two-dimensional electron gas, the shift of the distribution in the k space leads to non-equilibrium spin accumulation. To describe the ratio between the generated three-dimensional spin current

(J_s) and the injected two-dimensional charge current (j_e), a Rashba-Edelstein-effect coefficient (q_{REE}, in the unit of nm^{-1}) is introduced according to $\boldsymbol{J}_s = q_{REE}(\hbar/2e)\boldsymbol{j}_e \times \boldsymbol{\sigma}$.

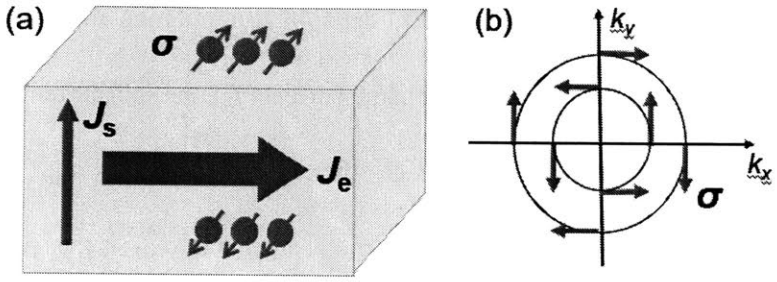

Fig. 1.4. Schematic of the spin Hall effect and the Rashba spin-orbit coupling. (a) The orthogonal orientation the charge current (J_e), the spin current (J_s), and the spin polarization (σ) in the spin Hall effect. (b) Helical Fermi contours with opposite spin polarizations due to the Rashba spin-orbit coupling.

Table 1.1. Spin transport parameters of heavy metals[26]

Materials	α_{SH}(%)	λ_{SD} (nm)
Pt	11	1.5
	8	1.5
	8	1.2
Ta	-2	1.8
Au	0.3	9.5
W	-0.43	1.5

1.4 Topological insulators

To obtain strong SOT effects, novel materials with more efficient charge-to-spin conversion are highly desired. Topological insulators are considered as a promising candidate due to their strong spin-orbit coupling. As illustrated in Fig. 1.5, an ideal topological insulator has conducting surface states and insulating bulk states. A Dirac dispersion cone is formed in the topological surface states, where the spin and the momentum of electrons are one-to-one locked to each other at the Fermi level. A flow of charge current can induce a large non-equilibrium spin accumulation and thus a highly polarized spin current[27-31]. Compared with the Rashba states which have two oppositely-spin-polarized Fermi contours, the topological surface states with the one-to-one locking can generate more significant non-equilibrium spin accumulation.

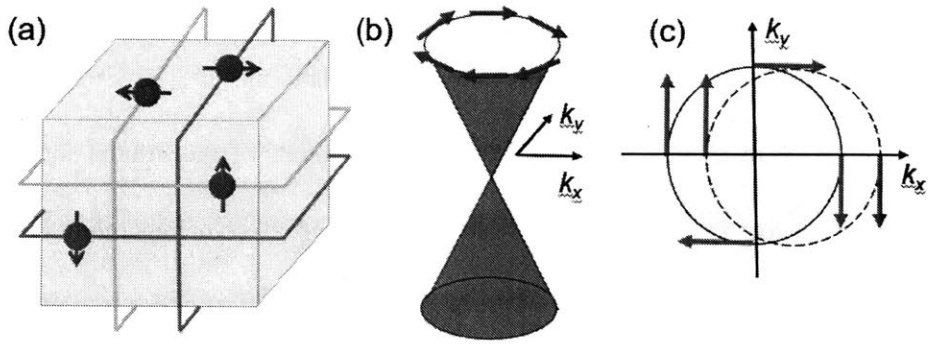

Fig. 1.5. Schematic of the electron structures in topological insulators. (a) Conducting surface states in an ideal topological insulator. (b) Dirac dispersion cone in the topological surface states, where the spin and the momentum of electrons are one-to-one locked to

each other at the Fermi level. (c) Top view of the Dirac cone crossed by the Fermi level with spin-momentum locking. With a flow of charge current charge current, the shift of the distribution in k space induces large non-equilibrium spin accumulation.

Recently, extraordinary charge-to-spin conversion efficiency in topological insulators has been demonstrated by various methods including spin pumping[31-34], spin torque ferromagnetic resonance[29,35,36], second harmonic magnetometry[37,38], non-local spin valve or tunnel junction[30,39-42], and spin Seebeck effect measurements[43]. The charge current through the topological insulator can generate SOT and significantly manipulate the magnetic dynamics of the neighboring ferromagnetic layer, and the obtained effective spin Hall angle α_{SH} of topological insulators is by the order of magnitude larger than heavy metals. Moreover, current-induced magnetic switching has been observed in magnetically doped topological insulator heterostructures[37,38,44]. The threshold current density for switching is $10^4 \sim 10^6$ A/cm^2, much lower than that in heavy metals (10^7 A/cm^2). However, restricted by the low Curie temperature of the diluted magnetic topological insulator, the switching can only be realized at cryotemperature. Room temperature SOT switching, which lies at the heart of the applicative interests, remains to be demonstrated. On the other hand, the obtained α_{SH} by different methods vary by orders of magnitude[29-42] because of different sample quality, data fitting process, and interpretation of the detection methods, which obscures the fundamental understanding

of the SOT mechanism. Moreover, very controversial temperature dependencies of α_{SH} have been reported in different measurements. While some experiments show that the SOT efficiency decays with the increasing temperature[30,31,36,39], others suggest the immunity of the SOT to the temperature[29,33,34]. It becomes questionable whether the topologically protected electronic states are robust enough for room temperature applications. Therefore, a direct, definitive experimental evidence to illustrate the SOT switching efficiency of topological insulators at room temperature is highly desirable.

1.5 Outline of the thesis

In this thesis, we will integrate ferromagnetic electrodes with high Curie temperature with topological insulator Bi_2Se_3 to study the possible SOT switching at room temperature. A major difficulty to obtain topological insulator-based SOT switching at room temperature is the growth of ferromagnetic layers with appropriate magnetic anisotropy on topological insulators. It is known that the ferromagnetic layers with perpendicular magnetic anisotropy (PMA) allows the most concise device structure to demonstrate the SOT switching[15-17]. However, the magnetic anisotropy of the commonly used ferromagnetic materials such as Co and CoFeB strongly relies on interfacial conditions, which usually favors an in-plane orientation when grown on topological insulators. Comparatively, transition metal–rare earth ferrimagnetic alloys (e.g., Co_xTb_{1-x}) are more promising owing to their robust bulk PMA[45-47]. Noticeably, existing work identifies CoTb

as a useful material to detect the SOT switching and to calibrate the SOT efficiency[48]. In Chapter 2, the details of the growth and the fabrication of the Bi_2Se_3/CoTb devices will be introduced. And the characterization of crystalline structure and magnetic properties will be presented.

The experimental results will be discussed in detail in Chapters 3 and 4. Current-induced magnetic switching in Bi_2Se_3/CoTb at room temperature will be presented and compared with the SOT switching induced by heavy metals (Chapter 3). In the next step, we will carry out quantitative calibration of the SOT efficiency of topological insulators (Chapter 4). A more straightforward calibration method compared with the previous indirect measurements, current-induced shift of the hysteresis loop[49], will be utilized.

Besides demonstrating the robust SOT generated by topological insulators, we will address another important issue associated with topological insulators, the bulk and surface contributions to the SOT. We propose to employ another topological insulator with more insulating bulk states[50,51], $(Bi,Sb)_2Te_3$, as a control sample. The comparison of the SOT efficiency between Bi_2Se_3/CoTb and $(Bi,Sb)_2Te_3$/CoTb would be helpful to clarify the possible origins of the SOT generated by TI. Finally, the spin Hall angle and the power consumption during the magnetic switching are chosen as the comparison metrics to show the advantages of the topological insulators over the heavy metals.

2 Sample fabrication and characterization

2.1 Growth of the topological insulators: molecular beam epitaxy

Molecular beam epitaxy (MBE) is an important technique to grow epitaxial thin films of single crystals. It has been widely utilized in the semiconductor industry and become a fundamental tool for the studies in quantum materials and nanotechnologies. A solid source MBE has separated evaporation cells that contain different elements. The materials sublime slowly when the cells are heated up and the atoms are deposited on the substrates. Appropriate substrates, ultrahigh vacuum ($<10^{-8}$ Torr), and low deposition rates are the key to obtain high-quality epitaxial films.

In our work, the topological insulator thin films were prepared by Nitin Samarth's group at the Pennsylvania State University. The Bi_2Se_3 films were grown by MBE on 2-inch GaAs (111)A wafers at a substrate temperature of approximately 300 °C using thermal evaporation of high purity elemental Bi and Se from Knudsen cells. The growth rate was 0.8 quintuple layers per minute. Before taking the sample out to air, the films were capped with 13 nm thick Se to protect the surface[29,52]. The thickness of the Bi_2Se_3 film is determined to be 7.4 nm by the X-ray reflection. The width of the Bi_2Se_3 (006) reflection rocking curve is 0.13°. The films were also characterized by X-ray diffraction (XRD) (Fig. 2.1) and atomic force microscopy (AFM) (Fig. 2.2). As shown in Fig. 2.1, only expected beaks from the Bi_2Se_3 film and the GaAs substrate are detected in XRD,

which indicates the high quality of the epitaxial Bi_2Se_3 films. Fig. 2.2 shows the AFM image of a Se-capped Bi_2Se_3 film. The Se capping layer appears to be continuous without pinholes and the roughness is 0.41 nm. After removing the Se capping layer by heating the sample up to 250 °C for 1 hour in vacuum, we did another AFM measurement to check the surface of Bi_2Se_3 (Fig. 2.3). The triangular flakes suggest good epitaxial growth of the Bi_2Se_3 film. The root mean square value of the surface roughness is 0.65 nm.

Besides GaAs, InP have been considered as another good substrate for epitaxial growth of the Bi_2Se_3 films. However, the semi-insulating InP substrates become highly conducting after the ion etching, which is an indispensable step in the device fabrication. On the contrary, the GaAs substrates remain semi-insulating after etching. Therefore, GaAs substrates are chosen in our experiments.

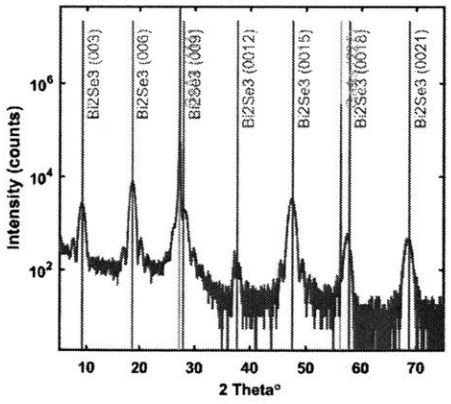

Fig. 2.1. XRD spectrum of the Bi_2Se_3 sample grown on GaAs (111)A substrate. The peaks of Bi_2Se_3 and GaAs are marked.

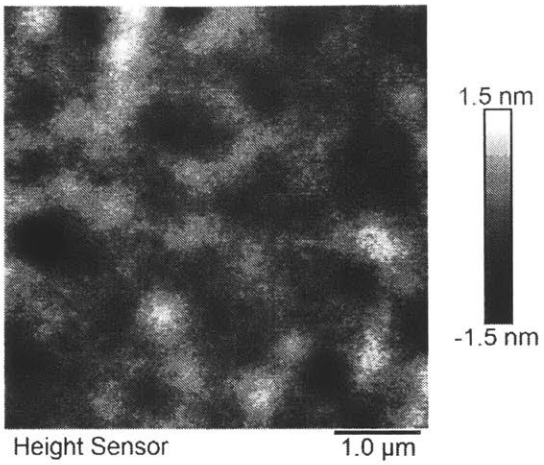

Fig. 2.2. AFM image of the Bi_2Se_3/GaAs sample with the capping layer of 13 nm thick Se. Se cap appears to be continuous without pinholes.

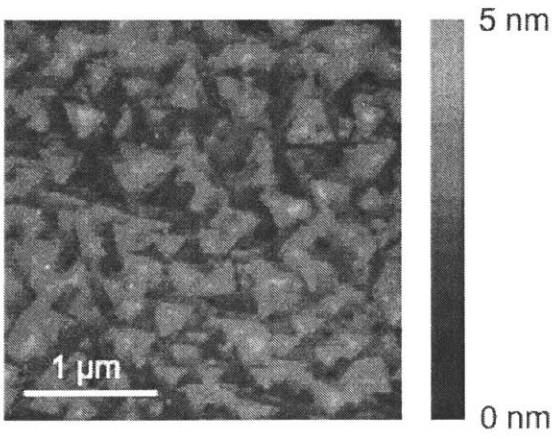

Fig. 2.3. AFM image of the Bi_2Se_3/GaAs sample after removing the capping layer of 13 nm thick Se.

2.2 Growth of the ferrimagnetic alloys: magnetron sputtering

Magnetron sputtering can be used to grow elemental or binary compound films with a wide range of thickness (from nanometers to microns). This technique has been industrialized and is compatible to back end of line fabrication technology. The targets are placed on the stages with magnets in the sputtering chamber. The chamber should reach a base pressure lower than 10^{-7} Torr to get high quality films and then filled with Ar gas. dc power source is used for deposition of electrically conducting materials, such as metals and alloys. A high voltage is applied between the target and the shell, which ignites the Ar plasma. The Ar ions are accelerated by the high electric fields and hit the target with the restriction of the magnetic fields. The atomic clusters escape from the surface of the targets and condense on the substrates to form the thin films.

In this work, the topological insulator samples were transferred via air to an AJA magnetron sputtering chamber with a base pressure of 6×10^{-9} Torr. The sample was firstly heated to 250 °C for 1 hour to remove the Se capping layer and cooled down to room temperature before deposition. A co-sputtering technique was employed to deposit CoTb alloys using separated Co and Tb targets at the Ar pressure of 2 mTorr. The power of Co was fixed at 100 W while that of Tb was varied to get different composition. Magnetic properties including anisotropy energy coefficient, coercivity, and saturation magnetization could be tuned within a wide range of values through thickness and

chemical composition engineering. After the growth of the CoTb layers, the samples were capped by a 3 nm thick SiN_x layer to protect the CoTb from oxidation.

2.3 Magnetic properties of CoTb alloy films

In $Co_{1-x}Tb_x$ alloys, the sublattices of Co and Tb elements are antiferromagnetically coupled due to the exchange interactions of d and f electrons. By increasing the atomic ratio of Tb, the magnetization changes from Co dominance to Tb dominance across a compensation point (x_0). When $x < (>) x_0$, the magnetic moments of Co (Tb) sublattice align parallel with the external field and the other is antiparallel (Fig. 2.4). At x_0 point, the magnetic moments of Co and Tb sublattices are fully cancelled with each other and the film shows rigidity to the external field. The compensated ferrimagnets not only maintain the basic properties of traditional antiferromagnets such as zero magnetic moment and the rigidity to external magnetic perturbations, but also show advantages in the aspect of magnetic state detection. It is known that probing the antiferromagnetic moments is one of the most challenging issues in antiferromagnet spintronics because of the cancellation of the equal sublattices. However, in transition metal–rare earth compensated ferrimagnets, despite zero magnetic moment, electrical transport and magneto-optic properties are uniquely determined by the transition metal sublattice because the Fermi level only crosses the transition metal sub-band. Therefore, the switching of Co and Tb moments can be directly detected through the anomalous Hall effect or the magneto-optic

Kerr effect[45-48]. Interestingly, recent experiments show the enhanced SOT efficiency[48,53-55] and the increased mobility of the magnetic domain wall motion[56] near the compensation point of ferrimagnetic alloys.

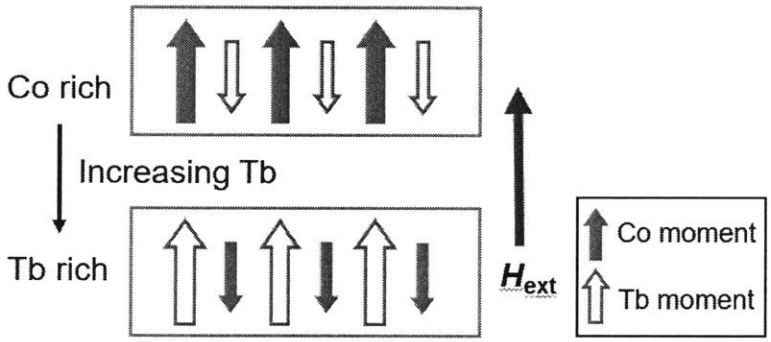

Fig. 2.4. Schematic of the magnetic moments in CoTb alloys. Co (Tb) moments are aligned parallel with the external field in Co (Tb) rich films and the other are antiparallel.

In order to detect the SOT switching, CoTb layers with relatively low thickness for small magnetic volume, strong PMA for sharp switching between up and down magnetic states by magnetic fields, and low coercivity would be favorable, which will result in a clear current-induced switching effect and a moderate switching current[57]. Unlike the commonly used ferromagnetic materials such as Co and CoFeB whose PMA strongly relies on interfacial conditions, the bulk PMA in CoTb is less sensitive to the interface, which can be enhanced by increasing the film thickness. However, we note that the thickness cannot be too large as both the magnetic volume and the coercivity increase

with the thickness. On the other hand, the magnetic properties show strong dependence on the chemical composition. When the composition is close to the compensation point, the low net magnetization reduces the in-plane anisotropy and assists the formation of PMA, which makes it possible to use a lower thickness. Unfortunately, the coercivity reaches maximum at the compensation point (infinite in the ideal case). Therefore, it is essential to find optimized materials parameters to balance the competitions among the aforementioned factors.

We grew a series of $Co_{1-x}Tb_x$ films with different composition and thickness and measured the out-of-plane magnetic hysteresis loops to find the optimal sample. The optimized parameters are $x = 0.23$ and thickness = 4.6 nm, which is in the Co-rich region. The hysteresis loop of this sample measured at room temperature is plotted in Fig. 2.5. The film shows moderate coercivity (< 300 Oe) and saturation magnetization (< 300 emu/cm^3) as well as strong PMA, which makes it possible to use the current-induced SOT to switch its magnetic moments.

The magnetic hysteresis loops were measured by the vibrating sample magnetometer (VSM). The VSM mains consists of a pair of split coils to apply magnetic fields and an electrical sensor to detect the induced electromotive force, which is generated by the vibrating magnetic sample via the Faraday effect. The electromotive force can be further converted to the magnetization of the measured sample.

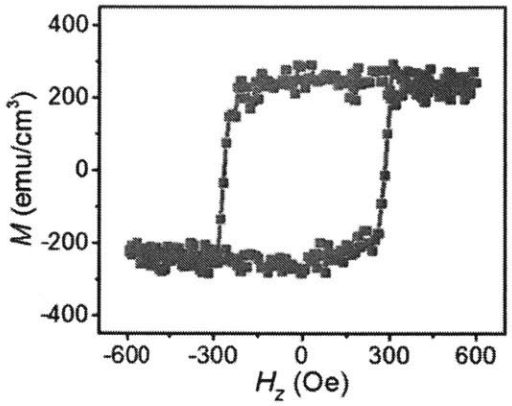

Fig. 2.5. Hysteresis loop of the out-of-plane magnetization in the Bi_2Se_3/CoTb sample measured by VSM at room temperature.

2.4 Device fabrication process

The detection of current-induced magnetic switching requires a concentrated charge current and therefore a well-defined current channel. We fabricated the sample to Hall-bar devices through the combination of photo-lithography and Ar ion milling. In photo-lithography, a photomask with designed patterns is used to cover the sample with photoresist. The photo resist under the transparent region of the photomask is exposed by ultraviolet rays and then removed by the liquid developer. The unexposed part covered by the patterns on the photomask remains to work as the shadow mask in the milling. The ion milling system generates high-speed flow of Ar ions through electrical acceleration, by which the materials can be etched away. The detailed process is described as follows.

i) Coating of the SPR-700 photoresist with a speed of 3000 round/min for 30 s, followed by a baking at 110 °C for 1 minute.

ii) Definition of the Hall bar. Expose the sample by ultraviolet rays for 7 s using the MA-4 aligner and the photomask. The width of the Hall bar is varied to be 4, 10, and 20 μm.

iii) Development of the photoresist in CD-26 developer for 40 s.

iv) Etching the sample using the Ar ion miller for 3 minutes. Use the multimeter to check whether the conducting films are completely removed.

v) Overnight soaking of the etched sample in acetone to remove the residual photoresist.

vi) Definition of the electrodes. Repeat steps ii and iii. Alignment of the patterns is needed.

vii) Etching the sample using the Ar ion miller for 0.5 minutes to remove the SiN_x.

viii) Deposition of the electrodes consisting of Ta (5nm)/Ru (30 nm) by magnetron sputtering, where Ta serves as the adhesion layer.

ix) Overnight soaking of the etched sample in acetone for lift-off.

2.5 Transport measurement

The magnetization reversal by either magnetic field or electrical current of the patterned devices was measured electrically via the anomalous Hall effect. A Keithley 2400 current source was used to provide dc current and an HP 3478A multimeter was

used to measure the transverse voltage to obtain the Hall resistance. An image of the device with the illustration of the measurement setup is shown in Fig. 2.6.

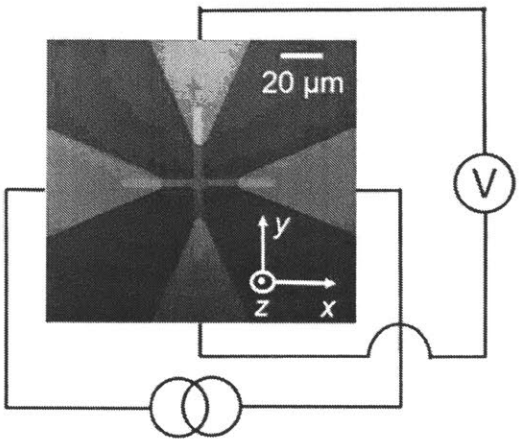

Fig. 2.6. Image of the Hall bar device with an illustration of the electrical measurement setup. The current is applied along the x axis and the Hall voltage is detected in the y direction. The width of the Hall bar is ~ 4 μm.

3 Current-induced switching by Bi_2Se_3

3.1 Anomalous Hall effect of Bi_2Se_3/CoTb samples

The electrons flowing through a conducting material under a perpendicular external magnetic field will deflect to the third orthogonal direction. This prominent effect, discovered by E. Hall in 1879[58], is well known as the ordinary Hall effect. In conducting ferromagnets, besides the ordinary Hall effect that scales linearly with the magnetic field, an additional term proportional to the magnetization also contributes to the total Hall resistance, which is named as the anomalous Hall effect[59]. In ferromagnets with strong PMA, the linear ordinary Hall component is usually negligible compared with the sharp switching of the anomalous Hall component. This effect is extensively used to electrically probe the magnetic states of conducting ferromagnetic materials.

In this work, the anomalous Hall effect in CoTb only depends on the magnetization of Co sublattices, because the position of Fermi level is at the Co sub-band. Fig. 3.1 shows the Hall resistance as a function of the out-of-plane magnetic field. The Hall resistance at zero field is 1.2 Ω. A sharp reversal can be seen at the field slightly higher than 200 Oe, which agrees well with the hysteresis loop in Fig. 2.5. Here we note that the magnetic properties of CoTb can be slightly changed during the fabrication process. Particularly, the heating can change the composition to more Co-rich regions.

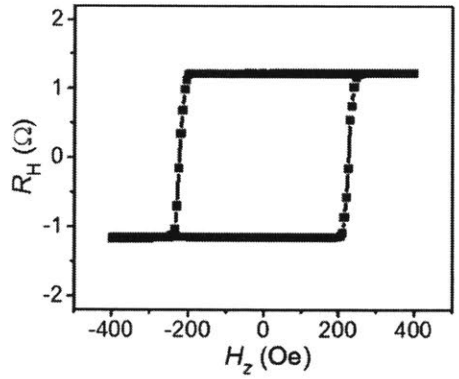

Fig. 3.1. Anomalous Hall effect (Hall resistance R_H vs out-of-plane magnetic field H_z) in the Bi_2Se_3/CoTb sample.

3.2 Current-induced switching in Bi_2Se_3/CoTb samples

In the heterostructure that contains spin-orbit material and ferromagnetic material with PMA, the damping-like term of the SOT $\boldsymbol{\tau}_{DL} \sim \boldsymbol{m} \times (\boldsymbol{\sigma} \times \boldsymbol{m})$ plays the dominant role in the magnetic switching. When the SOT competes over the torques induced by the external field $\boldsymbol{\tau}_{ext} \sim \boldsymbol{m} \times \boldsymbol{H}_{ext}$ and the anisotropy field $\boldsymbol{\tau}_{an} \sim \boldsymbol{m} \times \boldsymbol{H}_{an}$, the magnetic moments can be switched between up and down directions. An in-plane bias field along the current direction is necessary to obtain deterministic switching[57]. If the bias field is along + x axis (Fig. 3.2(a)), the magnetic moments are restricted in the right half plane and can be switched from up to down direction by a unidirectional charge current. With an opposite bias field, (Fig. 3.2(b)), the magnetic moments are restricted in the left half plane and can be switched from down to up direction by the same current and torque.

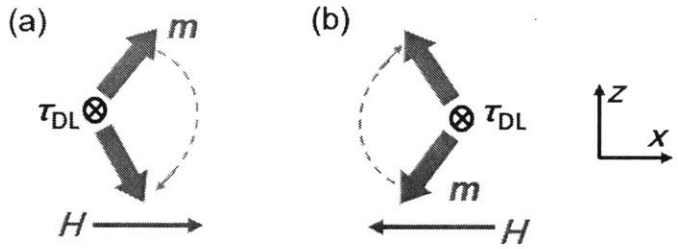

Fig. 3.2. SOT magnetic switching with the same current and torque, under the bias field along (a) $+x$ (b) $-x$ axis.

We now turn to studying the current-induced magnetic switching in Bi_2Se_3(7.4 nm)/CoTb(4.6 nm) bilayer at room temperature. The resistivities of the Bi_2Se_3 and the CoTb layers are determined to be 1060 and 97 μΩcm using four-point measurements, which is consistent with the measured total resistance of Bi_2Se_3/CoTb/SiN_x multilayer samples. The current density in Bi_2Se_3 can be calculated using a parallel circuit model. The Hall resistance is recorded to reveal the magnetic switching when sweeping a dc electrical current. An in-plane bias field of 1000 Oe is applied to get deterministic switching. As shown in Fig. 3.3, the current switches the magnetic moments of CoTb between up and states, corresponding to the Hall resistance of 0.6 Ω. The threshold current density for switching is 2.8×10^6 A/cm^2. The Hall resistance decreases at higher current because the Joule heating weakens the PMA. Moreover, the switching curve changes its polarity when the in-plane field is inversed, which is a typical characteristic of the SOT switching of PMA layers[57].

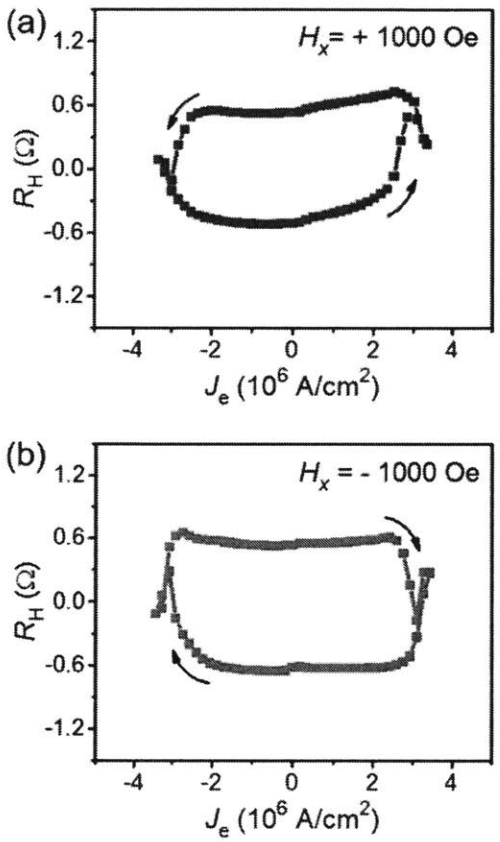

Fig. 3.3. Current-induced magnetic switching in the Bi_2Se_3/CoTb sample under a bias field of (a) + 1000 Oe and (b) – 1000 Oe along the current direction. The measurements were carried out at room temperature.

We notice that the Hall resistance at zero field is smaller than that in the field-induced switching shown in Fig. 3.1, which can be ascribed to the following two reasons. First of all, the anomalous Hall resistance in Fig. 3.1 is measured with the out-of-plane field only, while the current-induced switching is measured with an in-plane bias field of 1000 Oe, which tilts the magnetic moments to deviate from the perfect out-of-plane direction. For

quantitative comparison, we measure the Hall resistance as the out-of-plane field under an in-plane field of + 1000 Oe (Fig. 3.4). A small constant current is applied for resistance measurement but would not generate any scalable SOT. The Hall resistance at zero out-of-plane field is 0.7 Ω, very close to the results obtained by the current-induced switching (0.6 Ω, Fig. 3.3). Secondly, the magnetic moments in different regimes of the device are uniformly switched in the field sweeping measurements. On the contrary, due to the current spreading in the Hall branches, the charge current density is highly inhomogeneous at the cross-point of the Hall bar (Fig. 3.5). The current density at the edges of the cross section is lower than that at the channel center. As a result, the magnetic domains in these regions cannot be switched at the threshold current density during the current-induced switching. After taking these factors into consideration, our current-induced switching induced by Bi_2Se_3 is an almost full magnetic switching.

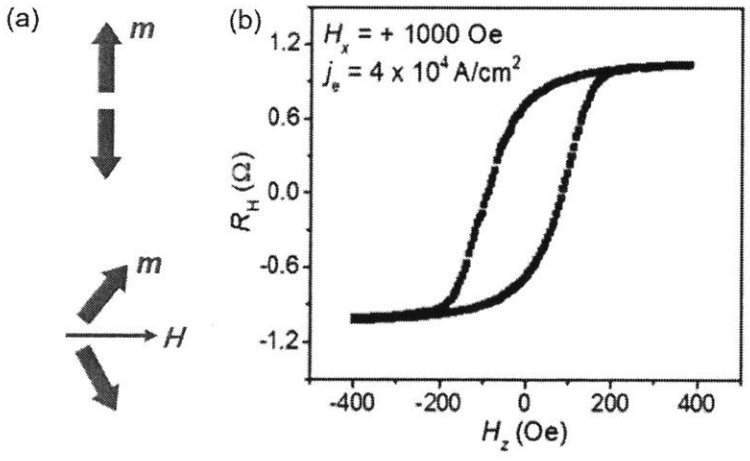

Fig. 3.4. Magnetic orientation in CoTb with PMA under an in-plane field. (a) Schematic of the magnetization of a PMA material under zero (upper panel) and finite (lower panel) in-plane field. (b) Hall resistance vs out-of-plane field measured in the Bi_2Se_3/CoTb sample, under an in-plane bias field of + 1000 Oe and a small constant current with the density of 4×10^4 A/cm^2.

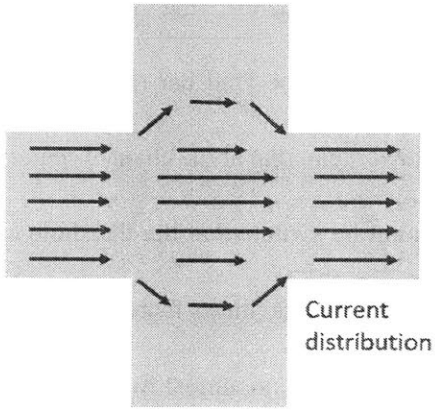

Fig. 3.5. Illustration of the inhomogeneous distribution of charge current in the cross section of the Hall bar device.

3.3 Comparison of the current-induced switching with heavy metals

To better understand the SOT switching induced by the topological insulator Bi_2Se_3, we also measured current-induced switching induced by heavy metals Pt and Ta. Pt(3 nm)/CoTb(2.1 nm)/SiN_x and Ta(5 nm)/CoTb(2.1 nm)/SiN_x samples were prepared. The resistivities of Pt and Ta are determined to be 23 and 193 μΩcm. The magnetic hysteresis loops were measured by VSM and plotted in Fig. 3.6. The coercivity is reasonable for

current-induce switching (~500 Oe for Pt/CoTb and ~60 Oe for Ta/CoTb). The saturation magnetization is 180 and 240 emu/cm^3, respectively.

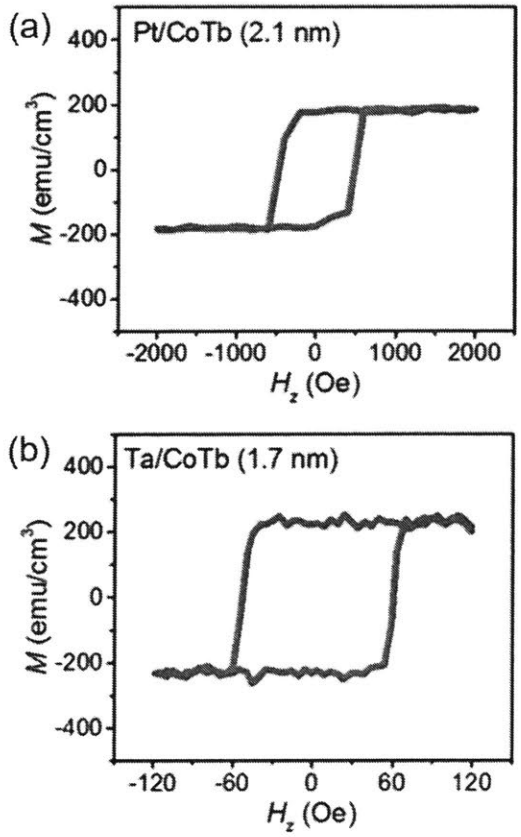

Fig. 3.6. Hysteresis loop of the out-of-plane magnetization in (a) Pt/CoTb and (b) Ta/CoTb samples measured by VSM.

Current-induced magnetic switching in Pt/CoTb and Ta/CoTb under positive in-plane fields were measured and plotted in Fig. 3.7. We can observe that the polarity of the switching curve with Bi_2Se_3 is the same as Pt but opposite to Ta. This indicates the sign

of the effective spin Hall angle of Bi_2Se_3, which corresponds to the direction of the current-induced spin accumulation, is the same as Pt but opposite to Ta. This also rules out the possibility that the spin-orbit coupling from the heavy element Tb plays the dominant role in the SOT switching, which will otherwise lead to the same switching polarity in all three samples. Furthermore, the threshold current density for switching with Bi_2Se_3 (2.8×10^6 A/cm^2) is much smaller than that with Pt (4×10^7 A/cm^2) and Ta (1×10^7 A/cm^2), even if the Bi_2Se_3/CoTb sample has the largest magnetic volume, which suggests the high efficiency of the charge-to-spin conversion in the topological insulator Bi_2Se_3.

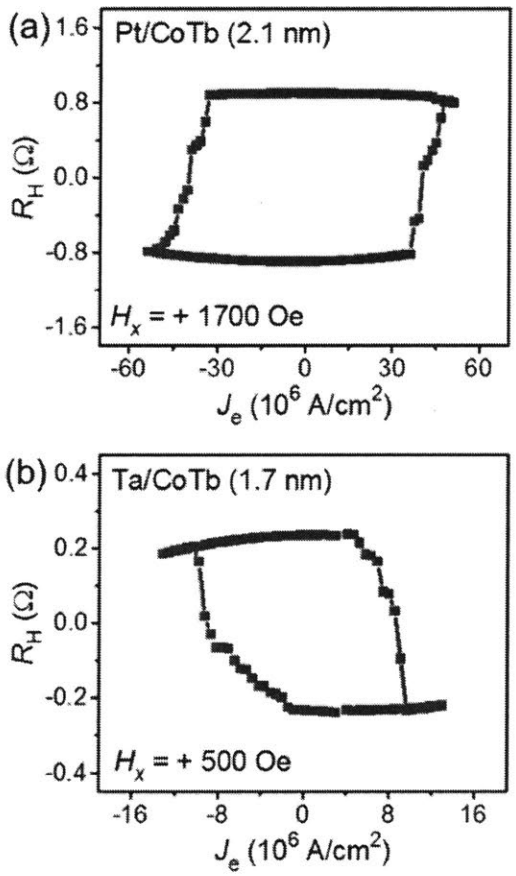

Fig. 3.7. Current-induced magnetic switching in (a) Pt/CoTb and (b) Ta/CoTb samples under positive bias fields along the current direction.

3.4 Review of recent work on SOT switching using topological insulators

In this section we will briefly review the existing results of the SOT switching induced by topological insulators. Fan *et al.* demonstrated for the first time that the Hall resistance can be reversed by a small amount of dc charge current in Cr-doped $(Bi,Sb)_2Te_3$ heterostructures[37,38]. Due to the low Curie temperature of the Cr-doped $(Bi,Sb)_2Te_3$, the switching was only observed at ~2 K. In 2017, Yasuda *et al.* showed the current-induced magnetic switching in similar structure with the replacement of the dc current by current pulses, which excludes the possible contributions of the current-nonlinear effects to the Hall resistance[44]. As to room temperature experiments, Mahendra *et al.* showed current-induced switching in perpendicularly magnetized sputtered-Bi_xSe_{1-x}/Ta/CoFeB multilayers[60]. The usage of sputtering technique in topological insulator growth may attract interest as it is more comparable to the semiconductor industry. Moreover, Bi_xSb_{1-x}-type topological insulators was demonstrated by Khang *et al.* to be an efficient SOT source through the switching measurements in epitaxial $Bi_{0.9}Sb_{0.1}$/MnGa bilayers[61]. Besides PMA materials, magnetic layers with in-plane anisotropy are also accompanied with topological insulators for switching detection. Wang *et al.* detected the current-induced magnetization reversal in Bi_2Se_3/NiFe through magneto-optic Kerr effect[62]. Unlike the SOT switching of PMA materials, in their work the anti-damping torque is

proposed as the origin of the magnetic switching. Despite different materials systems, these results as well as our work show that the topological insulators can induce efficient magnetic switching with the current density of $10^4 \sim 10^6$ A/cm^2.

4 Calibration of the SOT efficiency in topological insulators

4.1 Review of the methods to calibrate the SOT efficiency

The precise measurement of the SOT or the conversion between charge and spin currents is a central topic in the studies of spin-orbit physics. In the past few years, various methods have been utilized to subtract the merit of the charge-to-spin conversion, the spin Hall angle. Bauer and colleagues developed the method of spin pumping[63,64], where the ferromagnets at the ferromagnetic resonant condition can inject spin current to the adjacent heavy metal layer. Due to the inverse spin Hall effect, where a spin current with perpendicular spin polarization will be converted to a charge current in the third orthogonal direction, the spin Hall angle can be calculated by the ratio between the charge current and the spin current. Later, Liu *et al.* observed that the ferromagnetic resonance of a magnetic layer can be significantly influenced by the charge current in the adjacent heavy metal layer[65]. This is because the spin current generated by the spin Hall effect in the heavy metal layer exerts SOTs onto the magnetic moments. Both the field-like and the damping-like SOTs can be subtracted from the ferromagnetic resonance spectra. In 2014 this spin-torque ferromagnetic resonance was applied by Mellnik *et al.* to topological insulator/ferromagnetic metal structure[29], which is a pioneering work to demonstrate the SOT generated by topological insulators.

Besides high frequency experiments in which ferromagnetic resonance at several GHz is required, low frequency or dc measurements can also be applied to the SOT measurements. Kim *el al.* used the anomalous Hall resistance to reveal influence of the field-like and the damping-like SOTs on the magnetic moments through low-frequency harmonic measurements[66]. The field-like and the damping-like effective fields can be subtracted from the first and the second harmonic signals. In 2014, Fan *et al.* showed the ultrahigh charge-to spin-conversion ratio (> 400%) in magnetically doped topological insulator heterostructures using this harmonic method[37,38]. Similarly, dc measurement is also applicable by utilizing the planar Hall effect[60,67]. Moreover, non-local spin injection[30,39-41] or spin-polarized tunneling spectroscopy[42] as well as the spin Seebeck effect[43] have also been used to show the charge-to-spin conversion in topological insulators.

4.2 Current-induced shift of the hysteresis loop in Bi_2Se_3/CoTb samples

Given the discrepancy in the sample quality, the performing temperature, and the complex spin-orbit physics involved, the obtained spin Hall angles of topological insulators in previous works vary by orders of magnitude (from 10^{-3} to 10^{2}), which obscures the fundamental understanding of the SOT mechanism. In this work, we utilize a more straightforward method developed by Pai *et al.*, current-induced shift of the hysteresis loop[49], to calibrate the SOT efficiency. Compared with the previous indirect

measurements, this method is closely related to the magnetic switching scheme as it can directly probe the effective field for switching. The principle of this method in heavy metal/ferromagnetic metal bilayer is discussed as follows.

Unlike magnetic nanopillars with single magnetic domain, multiple domains with opposite magnetic orientations are formed in micrometer-size magnetic devices. The magnetic domain walls between two opposite domains paly the dominant role in the magnetic switching[49,68,69]. Due to the interfacial Dzyaloshinskii-Moriya interactions (DMI), Néel type domain walls with the same chirality are formed. The magnetic moments at the center of the up-down and down-up domain walls point to opposite directions. The damping-like SOT drives the domain walls to move towards the same direction with the same velocity, which can be described as a pair of effective magnetic fields with the same magnitude but opposite sign (Fig. 4.1(a)). When an external field is applied along the current direction, it competes with the DMI effective fields. As a result, the movement of up-down and down-up domain walls appears with different velocity, corresponding to domain expansion. The total effect of the damping-like SOTs in all the domain walls can be described by an out-of-plane effective field (Fig. 4.1(b)), which leads to an overall shift of the hysteresis loop. When the external field is large enough to overcome the DMI effective fields, the magnetic moments inside the domain walls tend to be aligned parallel with the external field. Consequently, the domain wall expansion has maximum velocity and the SOT efficiency reaches saturation. We note that although

this mechanism is described in ferromagnetic systems, it can also be applied to ferrimagnetic materials like CoTb[48,56].

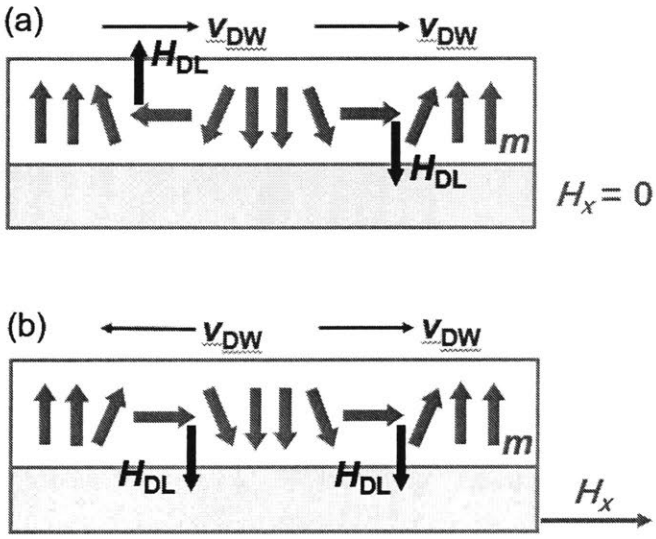

Fig. 4.1. Magnetic domain wall motion driven by the SOT under (a) zero and (b) finite in-plane bias field.

In order to measure the SOT effective field in the Bi_2Se_3/CoTb sample, we applied both a charge current and a magnetic field along x direction. At the same time, we swept the magnetic field along z direction (H_z) to measure the Hall resistance (R_H). As plotted in Fig. 4.2(a), under an in-plane bias field of H_x = + 800 Oe, the R_H vs H_z hysteresis loop shifts from zero to right and left in the presence of positive and negative charge current, respectively, where the SOT effective field (H_z^{eff}) is revealed by the deviation of the loop center from zero. The R_H vs H_z hysteresis loops were measured under a series of applied

current and H_x. H_z^{eff} as a function of the current density (j_e) is plotted in Fig. 4.2(b). The slope defined as $\chi \equiv H_z^{\text{eff}}/j_e$ represents the damping-like SOT efficiency, the sign of which depends on the direction of H_x.

We then summarize the SOT efficiency χ as a function of the in-plane bias field H_x in Fig. 4.2(c). At low field regions, χ grows linearly with H_x. This is consistent with the microscopic picture that magnetic domain walls tend to move with different velocity, resulting in domain expansion. When H_x exceeds a certain value ($H_x^{\text{sat}} \cong 200$ Oe), the SOT efficiency reaches its saturation (χ^{sat}) and remains unchanged, corresponding to the domain expansion with maximum efficiency. The effective spin Hall angle (α_{SH}, defined as the ratio between the generated spin current density $\frac{2e}{\hbar} j_s$ and the average charge current density in the spin-orbit layer j_e) of the Bi_2Se_3/CoTb heterostructure is calculated using[49]

$$\chi^{\text{sat}} = \frac{\pi}{2} \frac{\alpha_{\text{SH}} \hbar}{2e\mu_0 M_s t} \quad (1)$$

where $\hbar = 1.054 \times 10^{-34}$J/s is Planck's constant, $e = 1.602 \times 10^{-19}$C is the electron charge, $\mu_0 = 4\pi \times 10^{-7}$H/m is the vacuum permeability, $M_s = 280$ emu/cm^3 is the saturation magnetization obtained from Fig. 2.5, and $t = 4.6$ nm is the thickness of the CoTb layer. With $\chi^{\text{sat}} = 6.1 \times 10^{-6}$ Oe A^{-1}cm^2 obtained in Fig. 4.2(c), the effective spin Hall angle is determined to be 0.16 ± 0.02.

The DMI energy density D can also be estimated from the saturation bias field (H_x^{sat}) using[48] $D = H_{\text{DMI}} M_s t \mu_0 \Delta \cong H_x^{\text{sat}} M_s t \mu_0 \Delta$. The domain wall width $\Delta = (A/K_u)^{1/2}$ can

be calculated using the reported exchange stiffness[70] $A \cong 1.4 \times 10^{-11}\mathrm{J/m}$ and the anisotropy energy $K_u = \frac{\mu_0 M_s (H_{an}+4\pi M_s)}{2} = 6.4 \times 10^4 \mathrm{J/m^3}$, where the anisotropy field H_{an} and the saturation magnetization M_s can be determined from magnetization curve. The value of D is calculated to be 0.38 pJ/m, comparable to that reported in Ta/CoTb systems[48]. Accompanied with theoretical evaluations[71,72], our result experimentally suggests the DMI in topological insulator/ferromagnetic metal heterostructures. In addition, we note that the DMI is not necessary to detect current-induced switching, because the in-plane bias field can convert Bloch type domain walls to chiral Néel type domain walls.

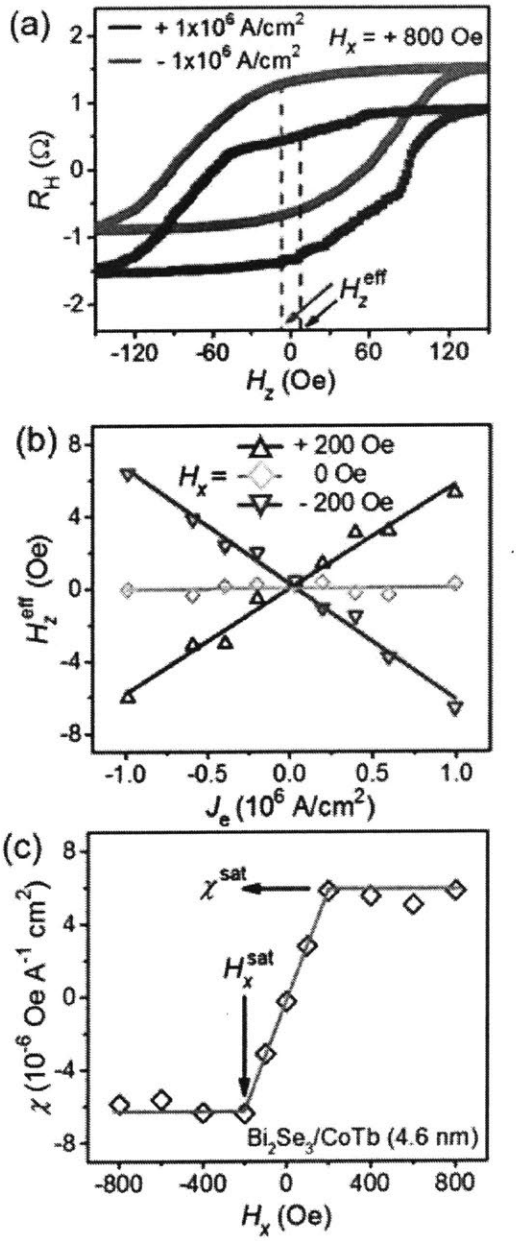

Fig. 4.2. Calibration of the SOT efficiency in the Bi_2Se_3/CoTb sample. (a) Hall resistance vs applied out-of-plane field under positive and negative dc currents with the density of 1.0×10^6 A/cm^2 through Bi_2Se_3 and a bias field $H_x = +800$ Oe. The center shift corresponds to the SOT effective field (H_z^{eff}). (b) H_z^{eff} as a function of applied current

under different bias fields $H_x = 0, \pm 200$ Oe. (c) SOT efficiency χ as a function of the bias field H_x. χ saturates at the field H_x^{sat}.

4.3 Comparison of the SOT efficiency with heavy metals

The SOT efficiency in Pt/CoTb and Ta/CoTb samples were also measured using the same method. Fig. 4.3 shows the SOT efficiency as a function of the in-plane bias field. Both results show similar characteristics with the Bi_2Se_3/CoTb, where the SOT efficiency firstly grows linearly with the bias field and then reaches saturation. As expected, the bias field along + x axis results in positive SOT efficiency in Bi_2Se_3/CoTb and Pt/CoTb, but negative efficiency in Ta/CoTb, which indicates that the spin Hall angle of Bi_2Se_3 has the same sign as Pt, but opposite to Ta. The spin Hall angles of Pt and Ta are calculated to be 0.017 ± 0.002 and -0.031 ± 0.002 using Eq. (1), much lower than that obtained in Bi_2Se_3/CoTb, which indicates the high charge-to-spin efficiency in topological insulators. Here we note that the values obtained in our experiments are smaller than some existing results[16,26,57]. We attribute this discrepancy to the low interfacial transparency[73] between the spin-orbit layer and the antiferromagnetically coupled alloy layer, which will reduce the spin current injected to the CoTb layer[48]. Nevertheless, by utilizing the same ferrimagnetic materials and calibration methods in all these measurements, we make sure that a fair comparison is made. In addition, it is noted that the saturation field that

corresponds to the DMI effective field in Pt/CoTb is much larger than that in Bi_2Se_3/CoTb and Ta/CoTb, which suggests the stronger DMI at the Pt/CoTb interface.

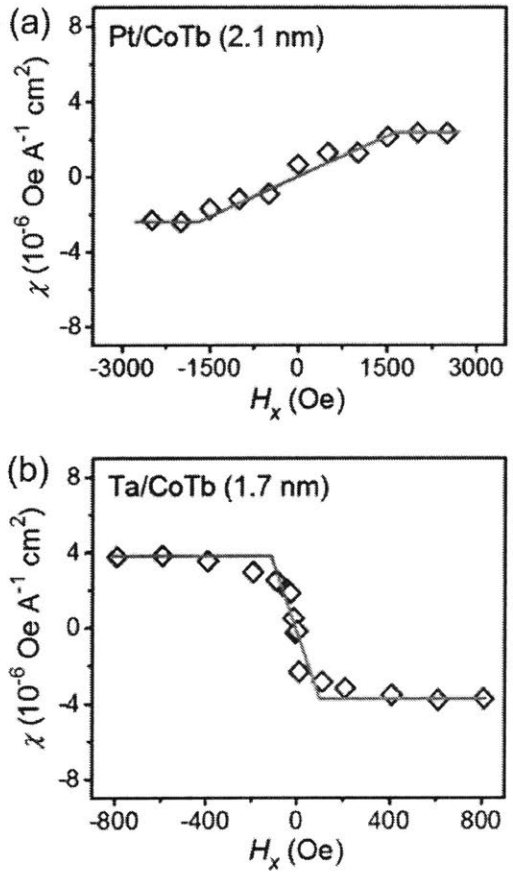

Fig. 4.3. SOT efficiency χ as a function of the bias field H_x in (a) Pt/CoTb and (b) Ta/CoTb samples.

4.4 Bulk and surface contributions to the SOT in topological insulators

Topological insulators are proposed to generate large non-equilibrium spin accumulation due to the spin-momentum locking at the topological surface states.

However, the bulk spin Hall effect is naturally involved due to the heavy elements in topological insulators such as Bi. It is nontrivial to separate the surface and the bulk contributions to the charge-to-spin conversion or the SOT, as both effects lead to the spin Hall angle with the same sign as Pt. This issue becomes more significant when dealing with Bi_2Se_3, as both surface states and conducting bulk states exist at the Fermi level. Experimentally, despite numbers of studies on the charge-to-spin conversion in different types of topological insulators, few of them have addressed this issue[31,32,34].

To get further insights on this topic, we employed another topological insulator with more insulating bulk states, $(Bi,Sb)_2Te_3$, as a comparison. By tuning the atomic ratio between Bi and Sb, the Fermi level of $(Bi,Sb)_2Te_3$ can be modified to stay in the band gap of the bulk states and cross the surface bands only, which has been verified by angle resolved photoemission spectroscopy[50,51]. This is also consistent with the electrical transport measurements[32,42] in previous and our experiments, where the resistivity of $(Bi,Sb)_2Te_3$ (4020 $\mu\Omega$cm) is determined to be 4 times larger than that of Bi_2Se_3 by 4 point measurements. Here we note that the conductivity of the bulk states in $(Bi,Sb)_2Te_3$ is reduced but not zero at finite temperature.

We grew a CoTb layer (8.0 nm, M_s = 300 emu/cm^3) with PMA on $(Bi,Sb)_2Te_3$ (8.0 nm). Due to the relatively large coercivity and thickness in this sample (Fig. 4.4), we were not able to detect the SOT magnetic switching. Alternatively, the SOT efficiency vs in-plane bias field was measured through the current-induced hysteresis loop shift, the same

method as the Bi_2Se_3 sample. The results plotted in Fig. 4.5 show the same trend as that of Bi_2Se_3. The effective spin Hall angle of $(Bi,Sb)_2Te_3$ is calculated to be 0.40 ± 0.04 according to Eq. (1), 2.5 times larger than that of Bi_2Se_3. The fact that topological insulators with reduced bulk conductance leads to higher spin Hall angle suggests that the topological surface states make significant contributions to the efficient SOT. Still, we would like to note that this comparison cannot completely exclude the bulk contributions.

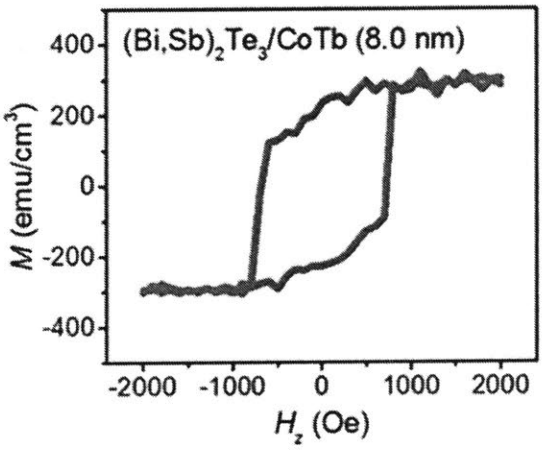

Fig. 4.4. Hysteresis loop of the out-of-plane magnetization in the $(Bi,Sb)_2Te_3$/CoTb sample measured by VSM.

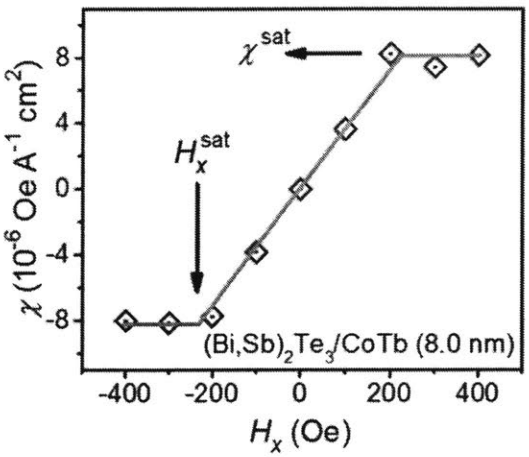

Fig. 4.5. SOT efficiency χ as a function of the bias field H_x in the $(Bi,Sb)_2Te_3$/CoTb sample.

The investigation of the bulk and surface contributions to the SOT can actually add insights to a more fundamental issue associated with topological insulators. It is known that the topological surface states are protected by the time inversion symmetry, which can be broken by a magnetic field. When the topological insulator is neighbored by a ferromagnet, the magnetic proximity effect may therefore have influence on the surface states. Some studies on the electron structures suggest that the surface states and the spin-momentum locking can be maintained with some tilting with the existence of magnetic impurities on the surface[74]. Our studies on the SOT switching and SOT efficiency in topological insulators provide further information on the spin-orbit interactions at the topological insulator/ferromagnet interface.

4.5 Summary of the switching parameters

Here we perform a summary and comparison of the SOT switching parameters with topological insulators and heavy metals. On one hand, the effective spin Hall angle of topological insulators is demonstrated much larger than that of heavy metals (Fig. 4.6 (a)), which identify topological insulators as a promising candidate to generate significant SOT. On the other hand, given the fact that topological insulators are more resistive than heavy metals, current-induced Joule heating in the SOT switching becomes a concern. We calculate the power consumption for switching ferromagnetic electrodes in unit magnetic volume, which is proportional to ρ/α_{SH}^2, as the heating is proportional to the resistivity of the spin-orbit material (ρ) and the critical current density for switching scales with the inverse of α_{SH}. As shown in Fig. 4.6(b), topological insulators still stand out as the favorable material when power consumption is used as the comparison metric. For further optimization the SOT efficiency, topological insulators with less conducting bulk states will be beneficial, as the current is mostly concentrated in the surface states with highly efficient charge-to-spin conversion and the dissipation in the bulk channel can be avoided. Finally, we note that in our current sample structure, the current shunting through the ferrimagnetic alloy layer is large. To fully exploit the SOT efficiency of topological insulators, magnetic semiconductors/insulators would be desired. Potential candidates include rare earth iron garnet or barium ferrite with PMA[75,76].

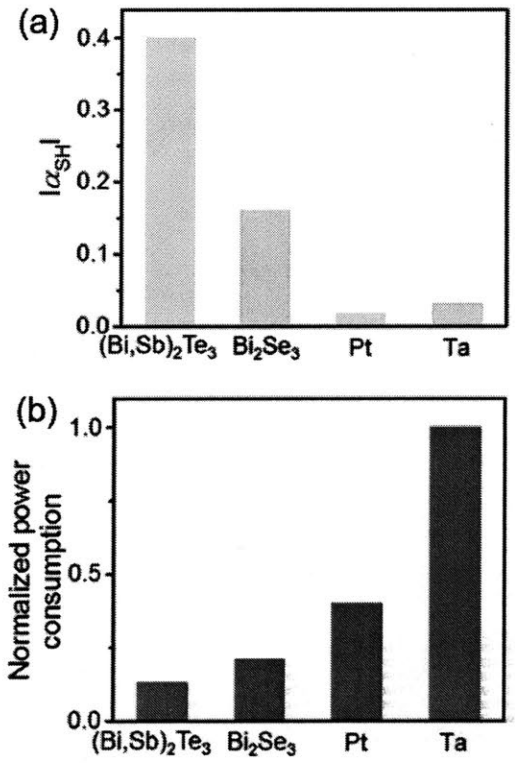

Fig. 4.6. Comparison of the SOT switching parameters with different spin-orbit materials. (a) Absolute values of the effective spin Hall angle of $(Bi,Sb)_2Te_3$, Bi_2Se_3, Pt, and Ta measured in our experiments. (b) Normalized power consumption (with Ta set to be unity) for switching ferromagnetic electrodes in unit magnetic volume using $(Bi,Sb)_2Te_3$, Bi_2Se_3, Pt, and Ta.

5 Conclusion

Here we summarize the main results achieved in this thesis.

i) SOT magnetic switching induced by the topological insulator Bi_2Se_3 is observed at room temperature.

ii) SOT efficiency of topological insulators and heavy metals are carefully calibrated using the current-induced hysteresis loop shift method.

iii) Topological insulators stand out as the favorable material when the spin Hall angle or the power consumption is used as the comparison metric.

iv) The comparison between Bi_2Se_3 and $(Bi,Sb)_2Te_3$ suggests the topological surface states make significant contributions to the efficient SOT.

Accompanied with recent SOT studies in topological insulators, our work adds to the technical significance of the emerging field of topological spintronics and potentially points to practicable innovations in topological insulator-based switching devices.

List of Figures

References

1. Wolf, S. A., Awschalom, D. D., Buhrman, R. A., Daughton, J. M., von Molnár, S., Roukes, M. L., Chtchelkanova, A. Y. & Treger, D. M. *Science* **294**, 1488–1495 (2001).
2. Chappert, C., Fert, A. & Van Dau, F. N. The emergence of spin electronics in data storage. *Nature Mater.* **6**, 813–823 (2007).
3. Baibich, M. N., Broto, J. M., Fert, A., Van Dau, F. N., Petroff, F., Etienne, P., Creuzet, G., Friederich, A. & Chazelas, J. Giant magnetoresistance of (001) Fe/(001) Cr magnetic superlattices. *Phys. Rev. Lett.* **61**, 2472–2475 (1988).
4. Binash, G., Grünberg, P., Saurenbach, F. & Zinn, W. Enhanced magnetoresistance in layered magnetic structures with antiferromagnetic interlayer exchange. *Phys. Rev. B* **39**, 4828–4830 (1989).
5. Moodera, J. S., Kinder, L. R., Wong, T. M. & Meservey, R. Large magnetoresistance at room temperature in ferromagnetic thin film tunnel junctions. *Phys. Rev. Lett.* **74**, 3273–3276 (1995).
6. Yuasa, S., Nagahama, T., Fukushima, A., Suzuki, Y. & Ando, K. Giant room-temperature magnetoresistance in single-crystal Fe/MgO/Fe magnetic tunnel junctions. *Nature Mater.* **3**, 868–871 (2004).
7. Parkin, S. S. P., Kaiser,C., Panchula, A., Rice , P. M., Hughes, B., Samant , M. & Yang, S.-H. Giant tunnelling magnetoresistance at room temperature with MgO (100) tunnel barriers. *Nature Mater.* **3**, 862–867 (2004).
8. Julliere, M. Tunneling between ferromagnetic films. *Phys. Lett. A* **54**, 225–226 (1975).
9. Ikeda, S., Hayakawa, J., Ashizawa, Y., Lee, Y. M., Miura, K., Hasegawa, H., Tsunoda, M., Matsukura, F. & Ohno, H. Tunnel magnetoresistance of 604% at 300 K by suppression of Ta diffusion in CoFeB/MgO/CoFeB pseudo-spin-valves annealed at

high temperature. *Appl. Phys. Lett.* **93**, 082508 (2008).

10. Slonczewski, J. C. Current-driven excitation of magnetic multilayers. *J. Magn. Magn. Mater.* **159**, 1–7 (1996).

11. Berger, L. Emission of spin waves by a magnetic multilayer by an electric current. *Phys. Rev. B* **54**, 9353–9358 (1996).

12. Sun, J. Z. Current-driven magnetic switching in manganite trilayer junctions. *J.Magn. Magn. Mater.* **202**, 157–162 (1999).

13. Huai, Y. Spin-transfer torque MRAM (STT-MRAM): challenges and prospects. *AAPPS Bulletin* **18**, 33–40 (2008).

14. Miron, I. M., Gaudin, G., Auffret, S., Rodmacq, B., Schuhl, A., Pizzini, S., Vogel, J. & Gambardella, P. Current-driven spin torque induced by the Rashba effect in a ferromagnetic metal layer. *Nature Mater.* **9**, 230–233 (2010).

15. Miron, I. M., Garello, K., Gaudin, G., Zermatten, P.-J., Costache, M. V., Auffret, S., Bandiera, S., Rodmacq, B., Schuhl, A. & Gambardella, P. Perpendicular switching of a single ferromagnetic layer induced by in-plane current injection. *Nature* **476**, 189–193 (2011).

16. Liu, L., Pai, C-F., Li, Y., Tseng, H. W., Ralph, D. C. & Buhrman, R. A. Spin-torque switching with the giant spin Hall effect of tantalum. *Science* **336**, 555–558 (2012).

17. Yu, G., Upadhyaya, P., Fan, Y., Alzate, J. G., Jiang, W., Wong, K. L., Takei, S., Bender, S. A., Chang, L.-T., Jiang, Y, Lang, M., Tang, J., Wang, Y., Tserkovnyak, Y., Amiri, P. K. & Wang. K. L. Switching of perpendicular magnetization by spin–orbit torques in the absence of external magnetic fields. *Nature Nanotech.* **9**, 548–554 (2014).

18. Dyakonov, M. I. & Perel, V. I. Current-induced spin orientation of electrons in semiconductors. *Phys. Lett. A* **35**, 459–460 (1971).

19. Hirsch, J. E. Spin Hall effect. *Phys. Rev. Lett.* **83**, 1834–1837 (1999).

20. Sinova, J., Valenzuela, S. O., Wunderlich, J. Back, C. H. & Jungwirth, T. Spin Hall

effect. *Rev. Mod. Phys.* **87**, 1213–1259 (2015).

21. Kato, Y. K., Myers, R. C., Gossard, A. C. & Awschalom, D. D. Observation of the spin Hall effect in semiconductors. *Science* **306**, 1910–1913 (2004).

22. Bychkov, Y. A. & Rashba, E. I. Properties of a 2D electron gas with lifted spectral degeneracy. *JETP Lett.* **39**, 78–81 (1984).

23. Edelstein, V. M. Spin polarization of conduction electrons induced by electric current in two-dimensional asymmetric electron systems. *Solid State Commun.* **73**, 233–235 (1990).

24. Manchon, A., Koo, H. C., Nitta, J., Frolov, S. M. & Duine, R. A. New perspectives for Rashba spin-orbit coupling. *Nature Mater.* **14**, 871–882 (2015)

25. Soumyanarayanan, A., Reyren, N., Fert, A. & Panagopoulos, C. Emergent phenomena induced by spin-orbit coupling at surfaces and interfaces. *Nature* ***539***, 509–517 (2016).

26. Wang, H. L., Du, C. H., Pu, Y., Adur, R., Hammel, P. C. & Yang, F. Y. Scaling of spin Hall angle in 3d, 4d, and 5d metals from $Y_3Fe_5O_{12}$/metal spin pumping. *Phys. Rev. Lett.* **112**, 197201 (2014).

27. Hasan, M. Z. & Kane, C. L. Colloquium: Topological insulators. *Rev. Mod. Phys.* **82**, 3045–3067 (2010).

28. Qi, X.-L. & Zhang, S.-C. Topological insulators and superconductors. *Rev. Mod. Phys.* **83**, 1057–1110 (2011).

29. Mellnik, A. R., Lee, J. S., Richardella, A., Grab, J. L., Mintun, P. J., Fischer, M. H., Vaezi, A., Manchon, A., Kim, E.-A., Samarth, N. & Ralph, D. C. Spin transfer torque generated by a topological insulator. *Nature* ***511***, 449–451 (2014).

30. Li, C. H., van't Erve, O. M. J., Robinson, J. T., Liu, Y., Li, L. & Jonker, B. T. Electrical detection of charge-current-induced spin polarization due to spin-momentum locking in Bi_2Se_3. *Nature Nanotech.* **9**, 218–224 (2014).

31. Shiomi, Y., Nomura, K., Kajiwara, Y., Eto, K., Novak, M., Segawa, K., Ando, Y. &

Saitoh, E. Spin-electricity conversion induced by spin injection into topological insulators. *Phys. Rev. Lett.* **113**, 196601 (2014).

32. Wang, H., Kally, J., Lee, J. S., Liu, T., Chang, H., Hickey, D. R., Mkhoyan, K. A., Wu, M., Richardella, A. & Samarth, N. Surface-state-dominated spin-charge current conversion in topological-insulator–ferromagnetic-insulator hetero-structures. *Phys. Rev. Lett.* **117**, 076601 (2016).
33. Jamali, M., Lee, J. S., Jeong, J. S., Mahfouzi, F., Lv, Y., Zhao, Z., Nikolic, B. K., Mkhoyan, K. A., Samarth, N. & Wang, J.-P. Giant spin pumping and inverse spin Hall effect in the presence of surface and bulk spin-orbit coupling of topological insulator Bi_2Se_3 *Nano Lett.* **15**, 7126–7132 (2015).
34. Rojas-Sánchez, J.-C., Oyarzún, S., Fu, Y., Marty, A., Vergnaud, C., Gambarelli, S., Vila, L., Jamet, M., Ohtsubo, Y., Taleb-Ibrahimi, A., Le Fèvre, P., Bertran, F., Reyren, N., George, J.-M. & Fert, A. Spin to charge conversion at room temperature by spin pumping into a new type of topological insulator: α-Sn Films. *Phys. Rev. Lett.* **116**, 096602 (2016).
35. Kondou, K., Yoshimi, R., Tsukazaki, A., Fukuma, Y., Matsuno, J., Takahashi, K. S., Kawasaki, M., Tokura, Y. & Otani, Y. Fermi-level-dependent charge-to-spin current conversion by Dirac surface states of topological insulators. *Nature Phys.* **12**, 1027–1031 (2016).
36. Wang, Y., Deorani, P., Banerjee, K., Koirala, N., Brahlek, M., Oh, S. & Yang, H. Topological surface states originated spin-orbit torques in Bi_2Se_3. *Phys. Rev. Lett.* **114**, 257202 (2015).
37. Fan, Y., Upadhyaya, P., Kou, X., Lang, M., Takei, S., Wang, Z., Tang, J., He, L., Chang, L.-T., Montazeri, M., Yu, G., Jiang, W., Nie, T., Schwartz, R. N., Tserkovnyak, Y. & Wang, K. L. Magnetization switching through giant spin-orbit torque in a magnetically doped topological insulator heterostructure. *Nature Mater.* **13**, 699–704 (2014).

38. Fan, Y., Kou, X., Upadhyaya, P., Shao, Q., Pan, L., Lang, M., Che, X., Tang, J., Montazeri, M., Murata, K., Chang, L.-T., Akyol, M., Yu, G., Nie, T., Wong, K. L., Liu, J., Wang, Y., Tserkovnyak, Y. & Wang, K. L. Electric-field control of spin-orbit torque in a magnetically doped topological insulator. *Nature Nanotech.* **11**, 352–358 (2016).

39. Tang, J., Chang, L.-T., Kou, X., Murata, K., Choi, E. S., Lang, M., Fan, Y., Jiang, Y., Montazeri, M., Jiang, W., Wang, Y., He, L. & Wang, K. L. Electrical detection of spin-polarized surface states conduction in $(Bi_{0.53}Sb_{0.47})_2Te_3$ topological insulator. *Nano Lett.* **14**, 5423–5429 (2014).

40. Ando, Y., Hamasaki, T., Kurokawa, T., Ichiba, K., Yang, F., Novak, M., Sasaki, S., Segawa, K., Ando, Y. & Shiraishi, M. Electrical detection of the spin polarization due to charge flow in the surface state of the topological insulator $Bi_{1.5}Sb_{0.5}Te_{1.7}Se_{1.3}$. *Nano Lett.* **14**, 6226–6230 (2014).

41. Dankert, A., Geurs, J., Kamalakar, M., Charpentier, S. & Dash, S. Room temperature electrical detection of spin polarized currents in topological insulators. *Nano lett.* **15**, 7976–7981 (2015).

42. Liu, L., Richardella, A., Garate, I., Zhu, Y., Samarth, N. & Chen, Y.-T. Spin-polarized tunneling study of spin-momentum locking in topological insulators. *Phys. Rev. B* **91**, 235437 (2015).

43. Jiang, Z., Chang, C. Z., Masir, M. R., Tang, C., Xu, Y., Moodera, J. S., MacDonald, A. H. & Shi, J. Enhanced spin Seebeck effect signal due to spin-momentum locked topological surface states. *Nature Commun.* **7**, 11458 (2016).

44. Yasuda, K., Tsukazaki, A., Yoshimi, R., Kondou, K., Takahashi, K. S., Otani, Y., Kawasaki, M. & Tokura, Y. Current-nonlinear Hall effect and spin-orbit torque magnetization switching in a magnetic topological insulator. *Phys. Rev. Lett.* **119**, 137204 (2017).

45. Buschow, K. H. J. Magnetic properties of amorphous rare-earth–cobalt alloys. *J.*

Appl. Phys. **51**, 2795–2798 (1980).

46. Choe, Y. J., Tsunashima, S., Katayama, T. & Uchiyama, S. Magneto-optic Kerr spectra of amorphous RE-Co thin films. *J. Magn. Soc. Jpn.* **11**, 273–276 (1987).
47. Hansen, P., Clausen, C., Much, G., Rosenkranz, M. & Witter, K. Magnetic and magneto-optical properties of rare-earth transition-metal alloys containing Gd, Tb, Fe, Co. *J. Appl. Phys.* **66**, 756–767 (1989).
48. Finley, J. & Liu, L. Spin-orbit-torque efficiency in compensated ferrimagnetic cobalt-terbium alloys. *Phys. Rev. Appl. 6*, 054001 (2016).
49. Pai, C. F., Mann, M., Tan, A. J. & Beach, G. S. D. Determination of spin torque efficiencies in heterostructures with perpendicular magnetic anisotropy. *Phys. Rev. B* **93**, 144409 (2016).
50. Zhang, Y., He, K., Chang, C.-Z., Song, C.-L., Wang, L.-L., Chen, X., Jia, J.-F., Fang, Z., Dai, X., Shan, W.-Y., Shen, S.-Q., Niu, Q., Qi, X.-L., Zhang, S.-C., Ma, X.-C. & Xue, Q.-K. Crossover of the three-dimensional topological insulator Bi2Se3 to the two-dimensional limit. *Nature Phys.* **6**, 584–588 (2010).
51. Zhang, J., Chang, C. Z., Zhang, Z., Wen, J., Feng, X., Li, K., Liu, M., He, K., Wang, L., Chen, X., Xue, Q.-K., Ma, X. & Wang, Y. Band structure engineering in $(Bi_{1-x}Sb_x)_2Te_3$ ternary topological insulators. *Nature Commun.* **2**, 574 (2011).
52. Richardella, A., Zhang, D. M., Lee, J. S., Koser, A., Rench, D. W., Yeats, A. L., Buckley, B. B., Awschalom, D. D. & Samarth, N. Coherent heteroepitaxy of Bi_2Se_3 on GaAs (111)B. *Appl. Phys. Lett.* **97**, 262104 (2010).
53. Mishra, R., Yu, J., Qiu, X., Motapothula, M., Venkatesan, T. & Yang, H. Anomalous current-induced spin torques in ferrimagnets near compensation. *Phys. Rev. Lett.* **118**, 167201 (2017).
54. Ham, W. S., Kim, S., Kim, D.-H., Kim, K.-J., Okuno, T., Yoshikawa, H., Tsukamoto, A., Moriyama, T. & Ono, T. Temperature dependence of spin-orbit effective fields in Pt/GdFeCo bilayers. *Appl. Phys. Lett.* **110**, 242405 (2017).

55. Ueda, K., Mann, M., de Brouwer, P. W. P., Bono, D. & Beach, G. S. D. Temperature dependence of spin-orbit torques across the magnetic compensation point in a ferrimagnetic TbCo alloy film. *Phys. Rev. B* **96**, 064410 (2017).

56. Siddiqui, S. A., Han, J., Finley, J., Ross, C. A., Liu, L. Current-induced domain wall motion in compensated ferrimagnet. *Phys. Rev. Lett.* **121**, 057701 (2018).

57. Liu, L., Lee, O. J., Gudmundsen, T. J., Ralph, D. C. & Buhrman, R. A. Current-induced switching of perpendicularly magnetized magnetic layers using spin torque from the spin Hall effect. *Phys. Rev. Lett.* **109**, 096602 (2012).

58. Hall, E. H. On a New Action of the Magnet on Electric Currents. *Am. J. Math.* **2**, 287–292 (1879).

59. Hall, E. H. On the "rotational coefficient" in nickel and cobalt. *Philos. Mag.* **12**, 157–172 (1881).

60. Mahendra, D. C., Grassi, R., Chen, J.-Y., Jamali, M., Hickey, D. R., Zhang, D., Zhao, Z., Li, H., Quarterman, P., Lv, Y., Li, M., Manchon, A., Mkhoyan, K. A. Low, T. & Wang, J.-P. Room-temperature high spin-orbit torque due to quantum confinement in sputtered $Bi_xSe_{(1-x)}$ films. *Nature Mater.* https://doi.org/10.1038/s41563-018-0136-z (2018).

61. Khang, N. H. D., Ueda, Y. & Hai, P. N. A conductive topological insulator with colossal spin Hall effect for ultra-low power spin-orbit-torque switching. *Nature Mater.* https://doi.org/10.1038/s41563-018-0137-y (2018).

62. Wang, Y., Zhu, D., Wu, Y., Yang, Y., Yu, J., Ramaswamy, R., Mishra, R., Shi, S., Elyasi, M., Teo, K.-L., Wu, Y., & Yang, H. Room temperature magnetization switching in topological insulator-ferromagnet heterostructures by spin-orbit torques. *Nature Commun.* **8**, 1364 (2017).

63. Tserkovnyak, Y., Brataas, A. & Bauer, G. E. W. Enhanced Gilbert damping in thin ferromagnetic films. *Phys. Rev. Lett.* **88**, 117601 (2002).

64. Mosendz, O., Pearson, J. E., Fradin, F. Y., Bauer, G. E. W., Bader, S. D. & Hoffmann,

A. Quantifying spin Hall angles from spin pumping: experiments and theory. *Phys. Rev. Lett.* **104** 046601 (2010).

65. Liu, L., Moriyama, T., Ralph, D. C. & Buhrman, R. A. Spin-torque ferromagnetic resonance induced by the spin Hall effect. *Phys. Rev. Lett.* **106**, 036601 (2011).
66. Kim, J., Sinha, J., Hayashi, M., Yamanouchi, M., Fukami, S., Suzuki, T., Mitani, S. & Ohno, H. Layer thickness dependence of the current-induced effective field vector in Ta/CoFeB/MgO. *Nature Mater.* **12**, 240–245 (2013).
67. Kawaguchi, M., Shimamura, K., Fukami, S., Matsukura, F., Ohno, H., Moriyama, T., Chiba, D. & Ono, T. Current-induced effective fields detected by magnetotrasport measurements. *Appl. Phys. Express* **6**, 113002 (2013).
68. Emori, S., Bauer, U., Ahn, S. M., Martinez, E. & Beach, G. S. D. Current-driven dynamics of chiral ferromagnetic domain walls. *Nature Mater.* **12**, 611–616 (2013).
69. Emori, S., Martinez, E., Lee, K.-J., Lee, H.-W., Bauer, U., Ahn, S.-M., Agrawal, P., Bono, D. C. & Beach, G. S. D. Spin Hall torque magnetometry of Dzyaloshinskii domain walls. *Phys. Rev. B* **90**, 184427 (2014).
70. Turner, J. J., Huang, X., Krupin, O., Seu, K. A., Parks, D., Kevan, S., Lima, E., Kisslinger, K., McNulty, I., Gambino, R., Mangin, S., Roy, S. & Fischer, P. X-ray diffraction microscopy of magnetic structures. *Phys. Rev. Lett.* **107**, 033904 (2011).
71. Tserkovnyak, Y. & Loss, D. Thin-film magnetization dynamics on the surface of a topological insulator. *Phys. Rev. Lett.* **108**, 187201 (2012).
72. Nomura, K. & Nagaosa, N. Electric charging of magnetic textures on the surface of a topological insulator. *Phys. Rev. B* **82**, 161401 (2010).
73. Zhang, W., Han, W., Jiang, X., Yang, S. H. & Parkin, S. S. P. Role of transparency of platinum-ferromagnet interfaces in determining the intrinsic magnitude of the spin Hall effect. *Nature Phys.* **11**, 496–502 (2015).
74. Wray, L. A., Xu, S.-Y., Xia, Y., Hsieh, D., Fedorov, A. V., Hor, Y. S., Cava, R. J., Bansil, A. Lin, H. & Hasan, M. Z. A topological insulator surface under strong

Coulomb, magnetic and disorder perturbations. *Nature Phys.* **7**, 32–37 (2011).

75. Avci, C. O., Quindeau, A., Pai, C.-F., Mann, M., Caretta, L., Tang, A. S., Onbasli, M. C., Ross, C. A. & Beach, G. S. D. Current-induced switching in a magnetic insulator. *Nature Mater.* **16**, 309–314 (2017).
76. Li, P., Liu, T., Chang, H. C., Kalitsov, A., Zhang, W., Csaba, G., Li, W., Richardson, D., DeMann, A., Rimal, G., Dey, H., Jiang, J., Porod, W., Field, S. B., Tang, J. K., Marconi, M. C., Hoffmann, A., Mryasov, O. & Wu, M. Z. Spin-orbit torque-assisted switching in magnetic insulator thin films with perpendicular magnetic anisotropy. *Nature Commun.* **7**, 12688 (2016).